Effect of arteriolar distensibility on the lateral migration of liquid-filled microparticles flowing in a human arteriole

Phd El Jirari, Adil El Baroudi, Amine Ammar

Effect of arteriolar distensibility on the lateral migration of liquid-filled microparticles flowing in a human arteriole

Imane El Jirari
LAMPA, Arts et Metiers Institute of Technology
49035 Angers, France
imane.eljirari@ensam.eu

Adil El Baroudi
LAMPA, Arts et Metiers Institute of Technology
49035 Angers, France
adil.elbaroudi@ensam.eu

Amine Ammar
LAMPA, Arts et Metiers Institute of Technology
49035 Angers, France
amine.ammar@ensam.eu

A promising advance of bioengineering consists in the development of micro-nanoparticles as drug delivery vehicles injected intravenously or intraarterialy for targeted treatment. Proficient functioning of drug carries is conditioned by a reliable prediction of pharmacokinetics in human as well as their dynamical behavior once injected in blood stream. In this study we aim to provide a reliable numerical prediction of dynamical behavior of microparticles in human arteriole focusing on the crucial mechanism of lateral migration. The dynamical response of the microparticle upon blood flow and arteriolar distensibility is investigated by varying main controlling parameters: viscosity ratio, confinement and capillary number. The influence of the hyperelastic arteriolar wall is highlighted through comparison with an infinitely rigid arteriolar wall. The hydrodynamic interaction in a microparticle train is examined. Fluid-structure interaction is solved by the Arbitrary Lagrangian Eulerian method using the COMSOL Multiphysics software.

Keywords: Human arteriole; arteriolar distensibility; lateral migration; microparticles; drug delivery.

1. Introduction

Microparticles are artificial microstructures used a drug delivery vectors [1,2] to remedy the limitations of chemotherapy and invasive treatments. Therapeutic applications include targeted treatment of cancerous tumour [3] and thrombus [4]. These microparticles consist of a thin-walled membrane made of lipid, protein or polymer enclosing a small amount of liquid drug and having common physical properties

with Red Blood Cell (RBC) and very similar dynamic in flow [5,6], enabling their use as a simplified model of RBC. The dynamical behavior of the drug carries and pharmacokinetic behavior of the coated drug is investigated in vivo [7] and in vitro [8]. The validation and optimisation of microparticles functioning to successfully meet higher therapeutic demands require a robust prediction of their dynamical behavior under blood flow and constraints imposed by vascular walls. The inertial lateral migration of microparticle in microfluidic devices in the absence of external force field is a physical phenomenon related to intrinsic hydrodynamical forces and channel geometry. The prominent microfluidic applications are bio-particle manipulation, particularly bioparticle fractionation (e.g. pinched flow fractionation and Dean flow fractionation [9]), filtration [10] and focusing [11]. Lateral migration is a relevant blood viscosity determinant in microvessels (diameter less than $500\,\mu$m) where RBCs migrates toward vessel centreline owing the creation of a cell-free layer, thereby decreasing the blood apparent viscosity (Fahræus effect). The lateral migration of microparticles in the absence of inertia or in finite inertia is an intriguing phenomenon that comes with broken microparticle symmetry (fore-aft asymmetric rigid microparticle or deformable microparticle). Numerous studies dealt with non-inertial lateral migration for artificial deformable microparticle [12,13] and for RBC [14]. The lateral migration of RBCs and artficial microparticles in a wall-bounded Poiseuille flow results from an interplay of four lateral forces: wall-induced lift force resulting from the disturbance of flow field induced by the presence of the microparticle and its reflection at the wall (the confinement induced repulsive wall force), shear-gradient lift force due to the curvature of undisturbed fluid velocity profile, Rubinow-Keller lift due to slip-rotation lift force and Saffman lift force due to the interaction of slip velocity and shear. Besides aforementioned lateral forces, a viscous drag acts in streamlines. Drag results from the relative velocity of the microparticle to the fluid. First revealed in [15], the deformability induced lift force is responsible of migration of elastic microparticles in the absence of inertia [16]. Deformability-induced lift is the key biomarker factor in malaria diagnosis since malaria-infected RBCs get stiffer and undergo a sidewalls margination while healthy RBCs migrates toward the centreline [17] (artificially hardened RBCs mimic the same behavior [18]). A controlling parameter in migration is the particle Reynolds number Re_p which determine if migration is of inertial or viscous origin. For particle Reynolds number much less than unity, viscous forces dominates and the microparticles drift from streamlines due to their asymmetry while for greater Re_p, the microparticle migrates due to inertial forces. The migration path, velocity and the equilibrium positions are found to depend on elastic properties of the microparticle [19,20], inertia [21,22], viscosity contrast between internal and external fluids [23,24], confinement [20,24] and on the initial microparticle position[25].

In [26], Beaucourt and co-workers have studied the migration of an artificial microparticle as a RBC simplified model confined in a capillary, for the sake of simplicity, authors limited the contribution of the deformable capillary wall to a local

elastic response. Authors had shown that the elastic capillary wall exerts a normal force compensating the lift force acting on the studied RBC model, guaranteeing equilibrium of the mechanical system. More recently in [27], authors had studied the effect of the arterial wall distensibility on deformation and velocity of a single microparticle, without any consideration of lateral migration. To our knowledge, apart from the two aforementioned studies none of published papers involve the contribution of vascular wall, let alone the influence of its complex mechanical behavior on lateral migration of microparticles. This paper aims to fill the lack of numerical studies on dynamical behavior of microparticle confined in blood vessels in literature, in particular on the migration process. To achieve this aim, the migration and the overall dynamical behavior are numerically investigated for a single isolated microparticle and for a train of three microparticles confined in a hyperplastic arteriolar wall and in an infinitely rigid arteriolar wall, while varying the confinement, the viscosity ratio and the capillary number. The numerical investigation is performed in COMSOL Multiphysics software package, the 2D fluid-structure interaction FSI non-linear problem is solved using the Arbitrary Lagrangian Eulerian method, with a monolithic approach.

2. Mathematical model

The computational domain (Figure 1), consists of a thin hyperelastic circular membrane enclosing an internal fluid, freely suspended in a confined external Poiseuille flow (blood). External and internal fluids are similar and the microparticle is neutrally buoyant since there is no contrast between both fluid densities. The idealized straight arteriole $L = 900$ μm is represented by a rectangular channel on which we distinguish the lumen (the interior space of the arteriole through which blood flows) $H_l = 30$ μm and surrounding arteriolar wall $H_a = 20$ μm. The coordinates of the centre of mass (x_c, y_c) are monitored over simulation. At the initial time, the microparticle is placed at $x_c/L = 0.5$ and $y_c/H_l = 0.27$. The inlet velocity v_i and the outlet normal stress are applied at (Γ_{i}) and at (Γ_{o}), respectively. Two FSI interfaces are identified : fluid domain-membrane (Γ_{fm}) and fluid-arteriolar wall (Γ_{fa}).

2.1. *Arteriolar wall*

Arterioles are muscular blood vessels that are able to dilate for purposes of regulate the vascular tone and maintain vascular permeability. Arteriolar wall comprises three layers (intima, media and adventitia) composed of smooth muscle cells, endothelial cells and collagen fibres. These components are dynamically interconnected making the frontiers blurred between the three layers. We limit the arteriolar wall to the inner layer (the intima) which is modeled as a nearly-incompressible hyperelastic material [28] following the neo-Hookean solid model (Eq. (3)). The equation

describing the motion of the arteriolar wall is given by :

$$\rho_a \frac{\partial^2 \mathbf{u}^{(a)}}{\partial t^2} = \nabla \cdot \boldsymbol{\sigma}^{(a)} \tag{1}$$

where $\rho_a = 960\ \left(\mathrm{Kg/m^3}\right)$ is the arteriolar wall density, $\mathbf{u}^{(a)}$ the displacement vector and $\boldsymbol{\sigma}^{(a)}$ the Cauchy stress tensor :

$$\boldsymbol{\sigma}^{(a)} = J^{-1}\mathbf{F}\,\frac{\partial W^{(a)}}{\partial \mathbf{E}^{(a)}}\,\mathbf{F}^T \tag{2}$$

Here J is the dilatation ratio, $\mathbf{F}$ the deformation gradient tensor, $\mathbf{E}^{(a)}$ the Green-Lagrange strain tensor and $W^{(a)}$ the strain energy density function whose nearly-incompressible form is written as

$$W^{(a)} = \frac{G^{(a)}}{2}\left(\bar{I}_{1,a} - 3\right) + \frac{\kappa}{2}\left(J-1\right)^2 \tag{3}$$

where $G^{(a)} = 6.2$ (MPa) is the shear modulus, $\bar{I}_{1,a}$ the first invariant of the isochoric right Cauchy-Green deformation tensor and $\kappa = 124$ (MPa) the initial bulk modulus. The deformable arteriolar wall that follows the neo-Hookean law (Eq. (3)) is denoted DAW while the infinitely rigid arteriolar wall is denoted RAW. roman.

2.2. *Blood flow*

In arteriolar blood circulation the shear rate exceeds 100 $\left(\mathrm{s^{-1}}\right)$ and blood is Newtonian [29]. In a physiological context, the Womersley number α measures the ratio of unsteady inertial forces to viscous forces, for $\alpha \leq 2$ unsteadiness is neglected and the flow is parabolic ($\alpha \leq 0.04$ in the arteriole), the profile is blunted (plug flow) for $\alpha \leq 10$ (see [30]). A fully-developed Poiseuille flow is imposed at the inlet of the arteriole

$$v_i = 4v_{\max}\frac{y}{H_l}\left(1 - \frac{y}{H_l}\right) \quad \text{at} \quad \Gamma_i\ (0 \leq y \leq H_l) \tag{4}$$

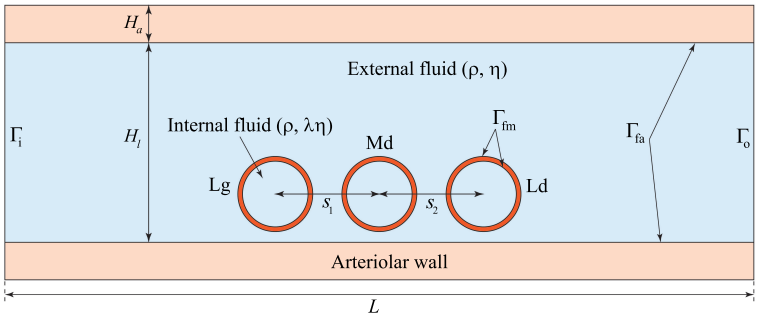

Fig. 1. Schematic drawing of the numerical model. Abbreviations Lg, Md and Ld denote the lagging, the middle and the leading microparticle, respectively. The single isolated microparticle configuration corresponds to an isolated middle microparticle.

where y is the ordinate. The maximum velocity $v_{\max} = 17$ (mm/s) located at $y = H_l/2$ is the peak velocity in human arteriol [31].

The fluids inside and outside microparticle are treated as incompressible, and therefore the mass conservation equation is written in the following form :

$$\nabla \cdot \mathbf{v} = 0 \tag{5}$$

Note that the presence of microparticle has no effect on the density and viscosity of the fluid phases inside and outside microparticle. In addition, the total stress in the fluid is expressed as :

$$\boldsymbol{\sigma} = -p\mathbf{I} + \eta \left[\nabla \mathbf{v} + (\nabla \mathbf{v})^T\right] \tag{6}$$

where p denotes the fluid pressure, $\mathbf{I}$ the identity tensor, $\mathbf{v}$ the velocity field and $\eta = 0.00345$ (Pa $\cdot$ s) the dynamic viscosity of the external fluid. The product $\lambda\eta$ denotes the internal fluid dynamic viscosity where $\lambda = 0.5 - 2$ is visosity ratio. Here the fluid domain is governed by the following Navier-Stokes equation in the absence of body forces :

$$\rho \left[\frac{\partial \mathbf{v}}{\partial t} + (\mathbf{v} \cdot \nabla)\, \mathbf{v}\right] = -\nabla p + \eta \nabla^2 \mathbf{v} \tag{7}$$

where $\rho = 1060$ $\left(\mathrm{kg/m^3}\right)$ is the fluid density.

2.3. *Microparticle*

The membrane is assumed to be homogeneous, isotropic, impermeable and incompressible. As in [32,33], the membrane is treated as a very thin hyperelastic surface of thickness h devoid of bending stiffness. With neglecting the bending stiffness, we consider that membrane deformation occurs only in-plane and thus the normal vector to the surface remains normal during the deformation. In the absence of bending moment, transverse shear forces vanishes. The bending of a membrane is primarily governed by two elastic parameters: its spontaneous (or preferred) curvature and its bending stiffness κ_b. For artificial microparticles with a thin homogeneous wall, the bending stiffness κ_b is directly related to the membrane thickness h :

$$\kappa_b = \frac{E^{(m)} h^3}{12(1-\nu^2)} \tag{8}$$

The dimensionless form proposed in[34] :

$$\tilde{\kappa_b} = \frac{h^2}{12(1-\nu^2)R^2} \tag{9}$$

$\tilde{\kappa_b}$ is the inverse of the Foppl-von Karman-number. The product $E^{(m)}h$ refers to surface Young modulus, R denotes the initial microparticle radius and ν the Poisson ratio. In this paper $\tilde{\kappa_b} = 0.0001$, this value is in concordance with experimental values of artificial microparticle membrane ($\tilde{\kappa_b} \simeq 0.00005 - 0.01$) [34,35] and with

RBC ($\tilde{\kappa_b} \sim 0.0001$) [34]. As in [20,36], the membrane hyperelasticity follows the strain-softening neo-Hookean law, which is found to appropriately model the mechanical behavior of protein-reticulated membranes [37]. Since the membrane is incompressible, Eq. (3) becomes :

$$W^{(m)} = \frac{G^{(m)}}{2}\left(\bar{I}_{1,m} - 3\right) \tag{10}$$

and Cauchy stress :

$$\boldsymbol{\sigma}^{(m)} = \mathbf{F}^{(m)}\,\frac{\partial W^{(m)}}{\partial \mathbf{E}^{(m)}}\,\mathbf{F}^{(m)^T} \tag{11}$$

Microparticle dynamics is controlled by dimensionless numbers: confinement $c = 2R/H_l$, particle Reynolds number $Re_p = \rho v_{\max} R^2/\left(\eta H_l\right)$ which gives the relative importance of intertial and viscous forces, viscosity ratio λ between the internal and the external fluids and the capillary number $Ca = \eta v_{\max}/G^{(m)}/h$ which measures ratio of viscous forces to the elastic resistance of membrane, the time in non-dimensionlized by the shear rate $t^* = \dot{\gamma} t$.

2.4. *Boundary conditions*

A zero-displacement constraint is applied at outer ends of arteriolar wall. The FSI pertaining the fluids satisfies the kinetic continuity

$$\begin{aligned} \mathbf{v} &= \frac{\partial \mathbf{u}^{(m)}}{\partial t} \quad \text{at} \quad \Gamma_{\text{fm}} \\ \mathbf{v} &= \frac{\partial \mathbf{u}^{(a)}}{\partial t} \quad \text{at} \quad \Gamma_{\text{fa}} \end{aligned} \tag{12}$$

representing mass conservation throughout the interface, and the FSI for the solids satisfies the dynamic continuity

$$\begin{aligned} \boldsymbol{\sigma} \cdot \mathbf{n} &= \boldsymbol{\sigma}^{(m)} \cdot \mathbf{n} \quad \text{at} \quad \Gamma_{\text{fm}} \\ \boldsymbol{\sigma} \cdot \mathbf{n} &= \boldsymbol{\sigma}^{(a)} \cdot \mathbf{n} \quad \text{at} \quad \Gamma_{\text{fa}} \end{aligned} \tag{13}$$

describing the equivalence of fluids stresses and solids stresses. Furthermore, let $\mathbf{v}_m$ denotes the dynamic mesh velocity and $\mathbf{n}$ the outer unit normal vector. At FSI interfaces mesh velocity satisfies

$$\mathbf{v}_m \cdot \mathbf{n} = \mathbf{v} \cdot \mathbf{n} \tag{14}$$

2.5. *Numerical method*

The ALE was developed to combine the advantages of the purely Eulerian description and the purely Lagrangian description (see [38]). The fundamental equation for ALE gives the variation of a physical quantity f for a given particle X as :

$$\frac{\partial f}{\partial t}|_X = \frac{\partial f}{\partial t}|_\chi + \frac{\partial f}{\partial x} \cdot \left(\mathbf{v}_m - \mathbf{v}\right) \tag{15}$$

where χ identifies referential gird coordinates and X denotes the spatial coordinates. The equations of the system are integrated over time using a first or second order accurate multistep implicit Backward Differentiation Formula scheme. The variables are updated at each time-step using a damped Newton nonlinear method [39]. The discretisation of the fluid domain is done with P2/P1 element that gives a quadratic basis for velocity and linear for pressure. In order to prevent numerical instabilities, two consistent stabilisation methods were introduced: streamline diffusion and crosswind diffusion. The first adds artificial diffusion in the streamline direction whereas the second adds diffusion in the cross direction. The mesh deformation is calculated using different nonlinear smoothing approaches : Winslow, Hyperelastic and Yeoh. The smoothing method is selected depending on divergence problem that occurs and element distorsion. Hyperelastic and Yeoh smoothing are both inspired by hyperelastic mechanical laws (neo-Hookean and Yeoh, respectively). A remeshing is automatically generated when mesh quality falls below a specified mesh quality threshold based on equiangular skewness or distortion.

3. Results and discussion

3.1. *Validation*

In this section we report the validation of the present numerical model by comparing our results to [20], where microparticle deformation is calculated using a mixed finite-difference/Fourier transform method for the flow solver and a front-tracking method for the deformable interface. The neo-Hookean membrane is incompressible and internal and external fluid are similar (Newtonian and incompressible). The microparticle is confined in a rigid microchannel and migrates upon a pressure-driven Poiseuille flow v_i :

$$v_i = -\frac{1}{2\eta}\frac{dp}{dx}\left(H_l y - y^2\right) \tag{16}$$

where dp/dx = cte is the pressure gradient and x the abscissa. The migration history is plotted over a range of capillary numbers $Ca = 0.1 - 0.8$ in Figure 2. The discrepancies in temporal evolution of migration between the present work and the work of [20]

$$\frac{|\text{Present} - \text{Ref. [20]}|}{\text{Ref. [20]}} \times 100$$

are presented in Table 1. Qualitatively, results are in excellent agreement with [20]. Quantitatively, discrepancies are found to increase with increasing microparticle stiffness (decreasing Ca) but remain acceptable (11.16% at most).

Table 1. Validation: comparison[a] of microparticle lateral position at specific dimensionless times.

	t^*				
Ca	2	4	6	8	10
0.1	0.38 %	2.88 %	5.63 %	8.44 %	11.16 %
0.2	0.71 %	0.82 %	1.94 %	3.37 %	4.97 %
0.4	1.13 %	0.57 %	0.18 %	0.78 %	1.40 %
0.8	0.03 %	0.71 %	0.04 %	0.35 %	0.19 %

[a] comparison with [20].

3.2. *Lateral migration in human arteriole*

3.2.1. *Lift and drag*

The lateral migration results from an intricate interplay of wall-induced lift f_W, shear-gradient induced lift f_{SG}, deformability induced lift force f_{Def}, deformable wall force f_{DW} and drag f_{drag}.

The wall exerts a repulsive translational force perpendicular to flow stream on the microparticle that is pushed away from the wall toward the centreline, this force is known as wall-induced lift f_W. The wall repulsive force originates from the stresslet field induced by the microparticle in presence of the wall [40] (the symmetric component of the first moment of the force per unit area at the microparticle surface). The stresslet contribution is decomposed into viscosity ratio contribution and particle shape contribution. In [41] authors had shown the existence of a viscoelatsic contribution in stresslet. The migration velocity near a rigid wall is inherently dependant on the stresslet since the migration velocity is the wall reflection of the

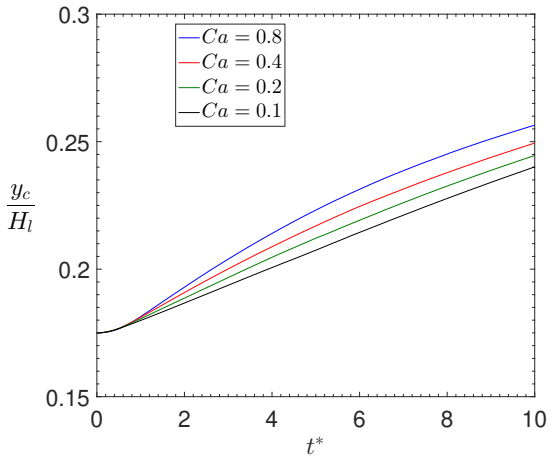

Fig. 2. Microparticle lateral migration history in a pressure-driven flow.

disturbance velocity (stresslet) of the spherical microparticle.

The migration away from the wall leads to a pressure gradient across the microparticle membrane and hence, in a relative velocity magnitude that is higher near the wall where the shear is maximal. This results in an extra lift force directed toward the nearest wall, known as shear-gradient lift force f_{SG}. The contribution of shear gradient is a function of the channel width and distance to the wall, with no dependence on the magnitude of the shear rate or the shear gradient [24].

Microparticle deformability takes indirectly part in migration via fore-aft symmetry breaking. The presence of the soft microparticle near the wall broke the fore-aft symmetry, thus permitting the micorparticle to undergo migration in Stokes flow[16]. The fore-aft asymmetry is a generic feature of living organisms and active matters systems that influence the collective and individual properties [42,43]. Due to the reversibility principle of Stokes equations, a single neutrally buoyant rigid microparticle fore-aft symmetric cannot undergo a lateral migration and remains at a unchanged distance from the wall. In contrast a single rigid fore-aft asymmetric shaped rigid microparticle is able to undergo a lateral migration (Purcell's scallop theorem for micro-swimmers). This theorem states that in a Newtonian fluid a time-reversible motion cannot produce any net force (lift) or net flow. However, in the presence of non-linear rheological fluid properties, a reciprocal swimming pattern can lead to a net displacement in a shear thinning/thickening) fluid [44] and in a viscoelastic fluid [45]. The deformability lift force is given by the analytical expression [46]

$$f_{Def} \propto \eta v_{\text{avg}} R \left(\frac{R}{H_l}\right)^2 \left(\frac{d}{H_l}\right) \tag{17}$$

Where v_{avg} is the average velocity. Here d denotes the distance between microparticle and vessel centreline. For the other lift forces, numerical values of Re_p and Ca used in this work are not within the range of validity of analytical expressions available in literature. The contribution of Saffman and Rubinow-Keller forces are neglected since the microparticle is neutrally buoyant [47,48] and the particle Reynlods numbers Re_p are much less than unity [11] ($Re_p \sim 10^{-3}$ and $\sim 10^{-2}$ for $c = 0.5$ and $c = 0.15$, respectively).

The drag arises from the difference in fore and aft velocities of the microparticle [49]. The wall induces a flow disturbance around the microparticle and tends to accelerate fluid around the microparticle increasing f_{drag} by a factor given by Faxen's correction (see [50]). The drag decays as the microparticle moves away from the wall (relative velocity decreases). Theoretical analysis of drag acting on deformable particle (bubble) is provided in [51].

3.3. *Single isolated microparticle*

3.3.1. *Deformation*

In response to the parabolic blood flow start the microparticle elongates in the streamlines direction and tilts. As Ca increases, the microparticle stiffness decreases and the microparticle is easily deformed. For $c = 0.5$ and for both arteriolar walls, this deformation enables the development of a pointy tail (cusp-like instability) at its rear-end and the tear-drop shape is observed for the DAW (Figure 3) and the RAW (Figure 4(a)). Since this cusp tend to extend closer to the wall, the microparticle is decelerated. As the microparticle moves away from the wall, the cusp relaxes and a roughly ellipsoidal shape is observed. At the vicinity of the centreline, the microparticle exhibits the famous slipper-shape (see Figure 3). The slipper shape observed for RBCs [52,53] and artificial microparticles [54], is found to results from a loss in stability of the symmetric shape [55] and allow the RBC to move faster in highly confined zones. The fore-aft asymmetry is much less pronounced for $c = 0.15$ and the microparticle remains roughly ellipsoidal. In fact, due to its size, the smallest microparticle moves at a greater distance from the RAW (even if at $t = 0$ both centers of mass are placed at the same distance to the wall), the influence of the RAW (i.e. asymmetry) on microparticle dynamic is consequently diminished.

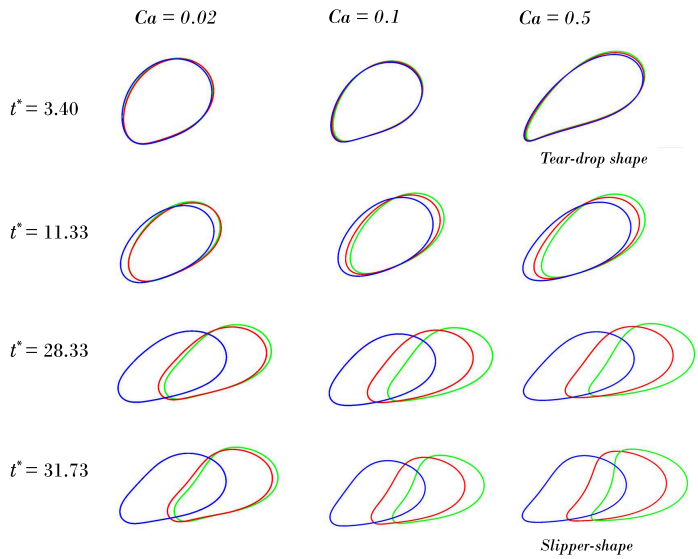

Fig. 3. Image sequence of deformed shapes at specific times for $c = 0.5$, DAW. Green color is for $\lambda = 0.5$, red for $\lambda = 1$ and blue for $\lambda = 2$.

3.3.2. *Migration*

In the presence of the DAW, the initially straight arteriole dilates and develops symmetrically an upper and a lower fusiform-liked bulges (Figure 5). The maximum arteriolar dilation is of 66% which is in the range of experimental values reported in[56] for human coronary arteriole. As a consequence of arteriolar dilation, the microparticle is temporarily downward aspired due to its vicinity with the lower wall, thereby, the migration is delayed (Figure 6) .

During the aspiration, f_{DW} and f_{SG} are prominent forces. The aspiration ends at $t^* = 2.5$ and $t^* = 15$ for $c = 0.5$ and $c = 0.15$, respectively, reflecting that the smallest micorparticle is more sensitive to wall distensibility (i.e. to f_{DW}). This effect becomes noticeable in Figure 6(d). For $c = 0.5$ the zone marking the transition from the aspiration to the effective migration get sharped as Ca increases (Figure 6(a)). Magnification of this zone reveals that the highest the Ca, the shortest the aspiration (Figure 6(b)). As shown in Figure 6(c), this trend is not observed for $c = 0.15$ and the effective migration is observed to start at a common threshold ($t^* = 15$). The influence of λ on migration alititude is accentauted for $c = 0.5$ and is shown to increases with Ca (see Figure 6(a)). In the presence of the RAW, the migration starts quasi-instantaneously. The smallest microparticle migrates quasi-linearly whilst the migration history shape of the largest one is similar to that of a logarithmic function (refer to Figures 6(a) and 6(c)). The plateau observed for different Ca corresponds to the equilibrium position morphologically indicated by stable deformation states (i.e. symmetrical parachute shape). The largest microparticle migrates beyond the arteriole centreline ($0.510 \leq y_c/H_l \leq 0.596$). Note that the centreline ($y_c/H_l = 0.5$) is not a stable equilibrium position since a little deflection will never return the microparticles back [57]. For both walls, the largest microparticle moves closer to the arteriole centreline. Regarding the influence of λ, obtained results confirm that λ restricts microparticles deformation and has an effect on the time required to reach the equilibrium shape (not on the equilibrium

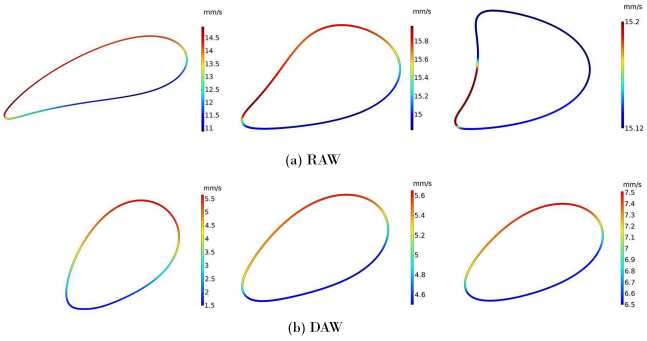

Fig. 4. Microparticle velocity magnitude ($\lambda = 2, c = 0.5, Ca = 0.5$) at $t^* = 1.7, 7.94$ and 15.86.

shape itself). The influence of λ on migration altitude increases with increasing Ca and c.

3.3.3. *Lateral velocity*

Lateral velocity or migration velocity V_y refers to y-component of membrane velocity. For $c = 0.5$, the "hook" in V_y time evolution in the presence of the RAW is due to f_{SG} that predominates other lift forces at early-times. Interestingly, in the presence of the DAW, V_y history is characterized by a "bump" as the microparticle migrates rapidly ($2.5 < t^* < 5$) before it decelerates (see Figure 7(a)). For $c = 0.15$ and as previously noticed, the smallest microparticle is more sensitive to f_{DW} and V_y evolves smoothly for both walls (RAW and DAW), expect for $t^* < 2.5$ where numerical instabilities are relatively important for DAW (Figure 7(b)). For both confinements, V_y tends to vanish as the microparticle moves closer to the equilibrium position.

3.4. *Microparticles train*

In this section we consider a train of three microparticles. The main purpose is to study the influence of the deformable wall on the hydrodynamic inter-particle interaction aiming to assess the risk of inter-particular clustering and/or microparticles adhesion/accumulation near the the wall and to clarify the interplay of main parameters in particle-to-particle dynamics for drug-delivery vectors design. Such situations could severely impede the blood stream and eventually, results in a non-targeted release of the drug, thus, toxifying healthy tissues. Let s_1 stands for the centroid-centroid distance between the middle and the lagging microparticle and

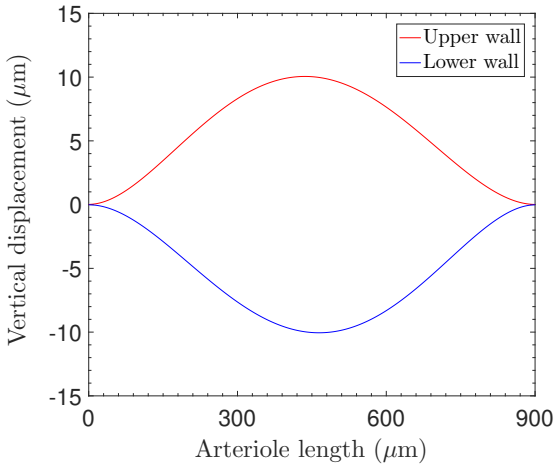

Fig. 5. Maximum arteriolar dilation.

s_2 the centroid-centroid distance between the middle and the leading microparticle (see Figure 1). At initial time both spacing are set to $s_1 = s_2 = 20$ (μm) and $s_1 = s_2 = 6$ (μm) for $c = 0.5$ and $c = 0.15$, respectively, keeping the ratio

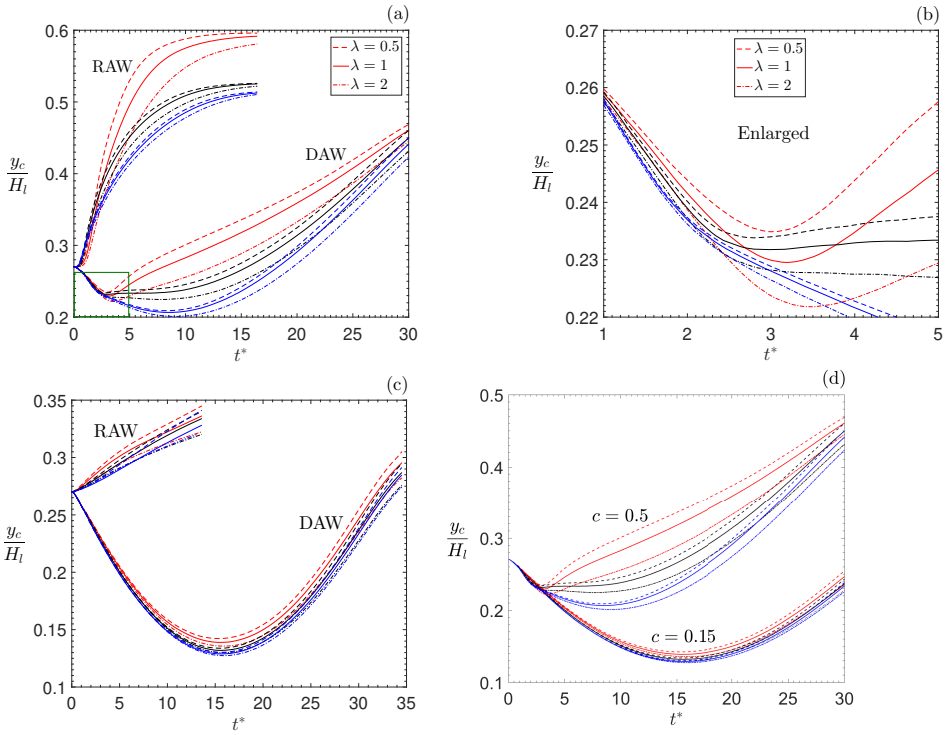

Fig. 6. Microparticle migration time evolution (a) $c = 0.5$ (b) $c = 0.15$ (d) DAW. Red color is for $Ca = 0.5$, black for $Ca = 0.1$ and blue for $Ca = 0.02$.

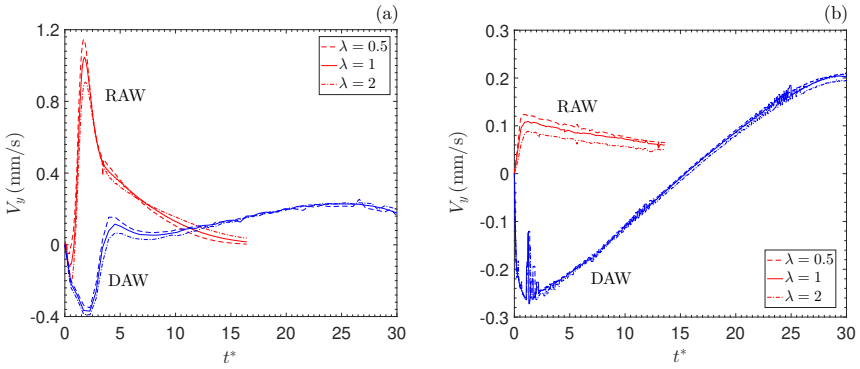

Fig. 7. Microparticle lateral velocity history (a) $c = 0.5$ and (b) $c = 0.15$.

$a/s_{1,2} = 0.75$ similar for both confinements. For ease of reading, the main results are presented and discussed separately for each confinement in dedicated subdivision ($c = 0.15$ and $c = 0.5$), each one is divided into two paragraphs, the first belongs to the migration/deformation and the second deals with the inter-particle spacing evolution. The section will be concluded by comments related to strain energy density.

3.4.1. $c = 0.15$

An intriguing mechanism is observed for all Ca and λ, the lagging microparticle overtook the middle one. This kinetic consists of an approach phase $t^* = 15 - 20$, a binary collision $t^* \approx 19.5 - 22.66$ and a separating phase $t^* \geq 24$ (Figure 8). During the approach phase isolines of pressure distribution has shown a high pressure area between both microparticles resulting in a repulsive force [58], this force combined with the microparticle position (the lagging microparticle experiences a high flow strength and hence moves faster) and microparticle size (due to its relative small size, the space is large enough to permit the overtaking process) is a propitious combination to this kinetic. During the binary collision, microparticles lose symmetry and their curvature vanishes at opposite faces (Figures 8(b)-(d)). The consecutive deformations observed during the binary collision are in excellent agreement with deformation of colliding cells in linear shear flow [36]. The overtaking behavior is indicated on curves by bumps mirrored to each other. For the lagging microparticle, the bumps widens with Ca while for the middle one, the bumps width seems to be independent on Ca (see Figure 9(a)). For both positions, the apparition of the bumps appears later as Ca decreases and the gap between the studied λ is diminished for $Ca = 0.1$. Upon closer examination of λ effect, for $Ca = 0.02$ and 0.1 the inflection point appears sooner for the less important λ and later for $\lambda = 2$. Conversely, the inflection in the bumps for $Ca = 0.1$ first occurs for $\lambda = 2$ followed by $\lambda = 0.5, 1$ (refer to Figure 9(b)).

Unlike the single isolated configuration, microparticles migrate non-linearly in the presence of the RAW and unexpectedly, the lagging microparticle hardly migrates. Its migration is even more difficult as Ca decreases and we observe a net aspiration (as in the presence of the DAW), suggesting that in this particular case f_W like f_{DW}, acts as a suction force (Figure 9(c)). Curiously for $Ca = 0.5$, the lagging microparticle combines upward and downward migration.

The lateral velocity of the leading microparticle evolves quiet similarly to that of the single isolated one, whichever the arteriolar rigidity (RAW or DAW). The same does not apply to the two other microparticles. For the RAW, the lateral velocity changes its monotony and this, more frequently for the lagging microparticle reaffirming its arduous upward migration (Figure 10(a)). As for the migration (i.e. mirror bumps) V_y time-evolution of the middle and the lagging microparticle are rough reflections to each other (Figure 10(b)). The inflections in each curve ($V_y = f(t^*)$) depict the balancing between the kinetic and the potential energies.

In the presence of the DAW, s_1 and s_2 diverge at $t^* = 10$. As for $c = 0.5$, s_2 manifest an exponential growth. For s_1, the curves slightly decrease with decreasing Ca till the overlapping at $t^* \approx 21.6$ (see Figure 8(c)) and starting from this point, they rise similarly to s_2. Plots shown in (Figure 11(a)) reveals less membrane shear resistance, less spacing growth. This influence is maintained but minimized for s_1 ($t^* \geq 21.6$). For the RAW, both spacing are growing with time (exponential or logarithmic-like growth) and are observed to expand the most with the highest Ca and the less for the intermediate Ca. In stark contrast to other studied combinations, s_1 widens more rapidly than s_2 (Figure 11(c)).

3.4.2. $c = 0.5$

Unsurprisingly, we found that the migration altitude is important for the leading microparticle (the middle microparticle is hampered by the presence of too microparticle on its both sides, the lagging one is restrained by too in-front microparticles) (see Figure 12). The discrepancies in middle and lagging migrations

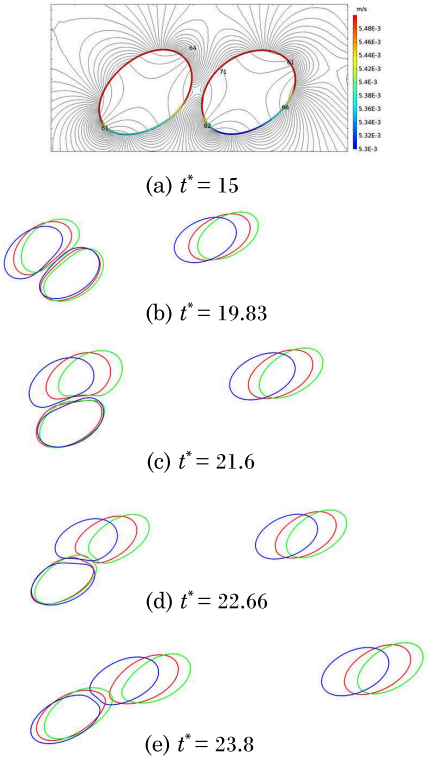

Fig. 8. Overtaking behavior ($c = 0.15$, $Ca = 0.5$, DAW) (a) Isolines of pressure contour at the approach phase, color legend is for microparticle velocity. (b)-(e) Sequential snapshots of overtaking, green color is for $\lambda = 0.5$, red for $\lambda = 1$ and blue for $\lambda = 2$.

are barely discernible. For the sake of conciseness, we confine ourselves to present the combination $Ca = 0.1$, $\lambda = 1$ in order to evaluate the risk of accumulation near the rigid wall. Plots in Figure 9(d) confirm the upward migration. Because of the important asymmetry, we chose to quantify the deformation of the microparticles through the deformation gradient $\mathbf{F}^{(m)}$ (instead of the geometric Taylor parameter) that gives information about the local deformation with respect to the non-deformed

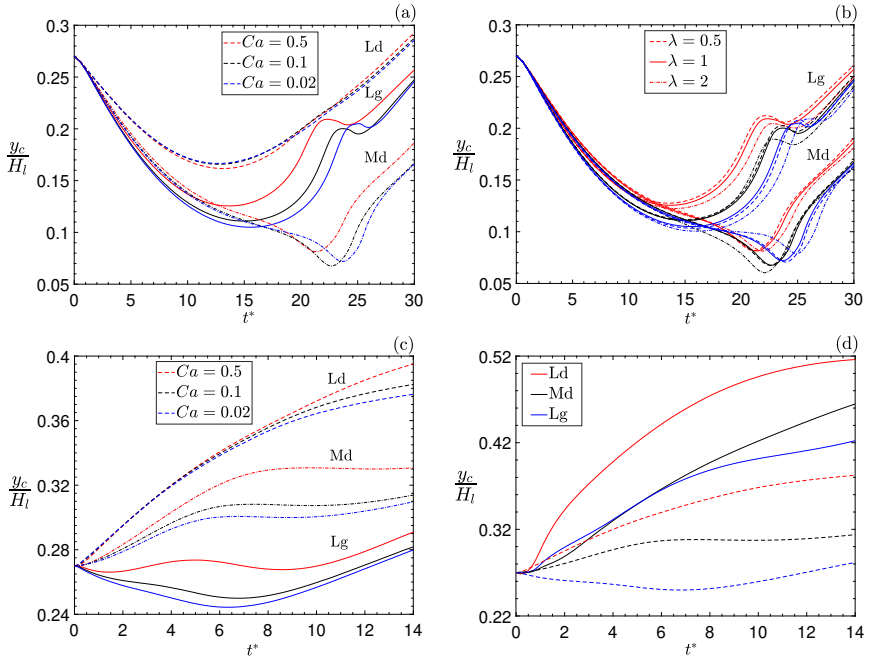

Fig. 9. Microparticles migration histories (a) ($\lambda = 1$, $c = 0.15$, DAW) (b) $c = 0.15$, DAW (c) ($\lambda = 1$, $c = 0.15$, RAW) (d) Solid lines are for $c = 0.5$ and dashed lines for $c = 0.15$ ($\lambda = 1$, RAW).

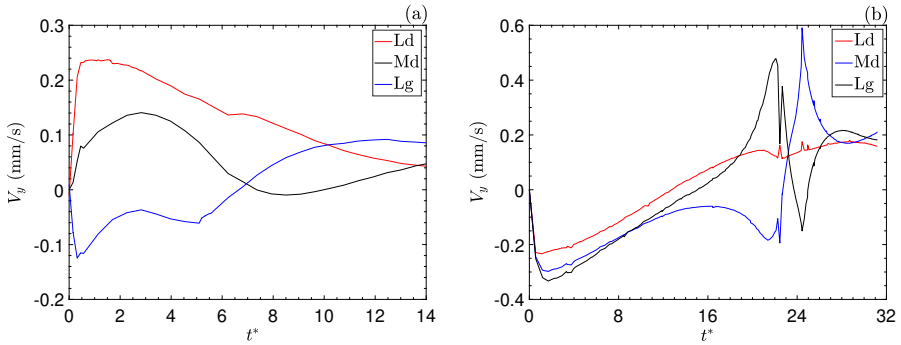

Fig. 10. Microparticles lateral velocity histories ($\lambda = 1$, $c = 0.15$, $Ca = 0.1$) (a) RAW (b) DAW.

(referential) state. The main result is microparticle's position influence on arteriolar wall rigidity effect. In fact, the divergence between the deformation gradients for each arteriolar rigidity model widens as the microparticle is placed far from the arteriole entrance (Figure 13). Qualitatively, quite a few uncommonly observed are characterizing morphological evolution of the largest microparticle. The middle microparticle develops a sharp cusp-like instability as a results to a combination of important softness, quasi-null bending rigidity, infinite wall rigidity and a favorable position. This important local deformation lead to the appearance of a singularity and hence, to convergence issues. We believe that the singularity is a consequence of infinite stress at the cusp that could be fixed by increasing the bending rigidity and/or modeling the membrane mechanical behavior using a strain-stiffening law (e.g. Skalak *al.* law), as both restrict microparticle deformation. We opt for a simpler alternative consisting in decreasing the capillary number to $Ca = 0.4$ (by increasing $G^{(m)}$). As for the single isolated configuration, the cusps relax with time (except for the singularity-related case). For $Ca \geq 0.4$, the lagging and middle microparticles

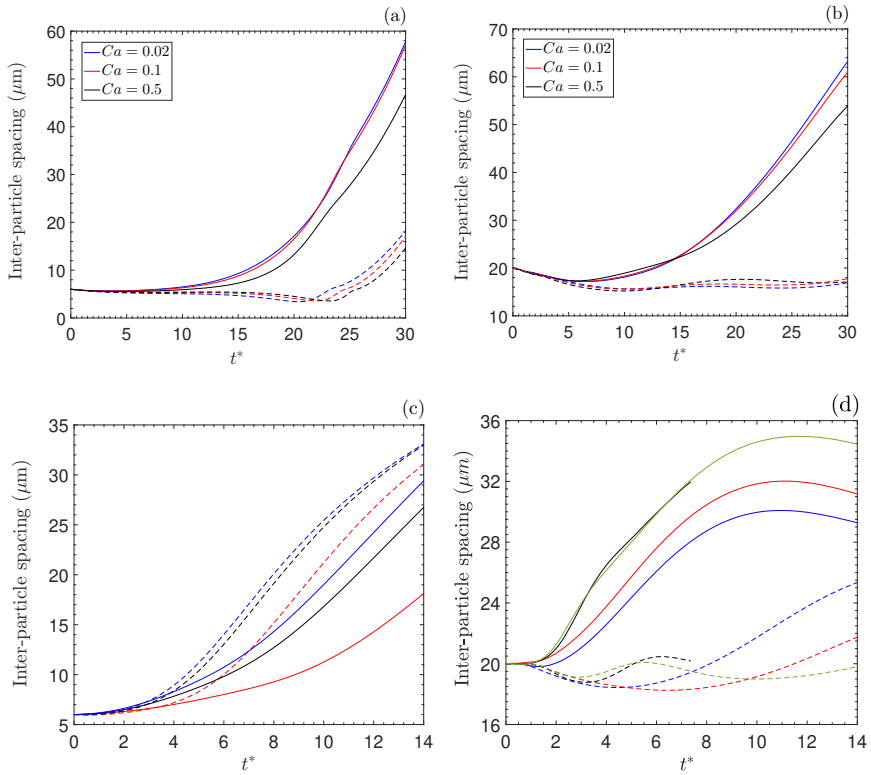

Fig. 11. Inter-particle spacing time evolution for $\lambda = 1$, dashed lines are for s_1 and solid ones for s_2 (a) $c = 0.15$, DAW (b) $c = 0.5$, DAW (c) $c = 0.15$, RAW (d) $c = 0.5$, RAW, green color is for $Ca = 0.4$.

flatten in a significant way in the immediate vicinity to the RAW, in addition to cusps formation (Figure 14). The flatness disappears progressively as microparticles move away from the wall. As illustrated in Figure 15, wall deformability also brings about a localized flatness and cusp formation, the novel observed behavior is the trend to 'raise' for $Ca = 0.5$ ($t^* = 4.53$) which relatively restricts the flattened zone in close contact to the wall. This deformation mode is propitious to lateral migration as it helps to circumvent the f_{DW} and the constraints imposed by narrow spacing from neighboring microparticles (i.e. hydrodynamic pressure). Besides giving information about morphological changes in microparticle shape, Figure 14 also serves to concretely describe the evolution of spacing s_1 and s_2 and to show the clustering while Figure 15 highlights the influence of Ca on microparticles lateral velocities.

In the presence of the DAW, s_1 and s_2 fall below 20 (μm) and diverge at $t^* = 5$, above this point, s_2 increase in an exponential fashion while s_1 evolve quasi-steadily and oscillate between 15.22 (μm) and 17.64 (μm). Apropos of the influence of Ca, it is observed that the higher Ca the less s_2, this influence is not obvious on s_1 (Figure 11(b)). As regards to the RAW, s_2 evolve in a concave fashion and in contrary to previously noticed for the migration of the lagging and the middle microparticles, the inflection points in s_2 evolution are found to occur sooner as Ca decreases. Surprisingly, the temporal evolution of s_1 and s_2 for $Ca = 0.4$ and $Ca = 0.5$ depict an outright concavity change (Figure 11(d)). The corresponding descending curves are a sign of microparticle clustering. Microparticle deformability plays a major role in clustering and in inter-particle spacing decrease. In fact, a hydrodynamic flow forces amount is absorbed by microparticle deformation, reducing the repulsive force that acts to keep microparticles apart. While the clustering of RBCs is protein-induced and results from an intricate balancing of "cross-bridging" and depletion forces [59], the clustering of artificial microparticles is due to the presence of ahead converging vortexes and rear diverging ones [60].

The elastic strain energy $W^{(m)}$ increases with microparticle deformability, thereby with elastic resistance [61] and microparticle position. The wall rigidity is observed to significantly increase $W^{(m)}$ since the flow strength is exclusively directed toward the microparticle which stores the elastic energy through deformation (Figure (17(a)). The temporal evolution of $W^{(m)}$ during the three phases composing the overtaking kinetic ($15 \leq t^* \leq 24$) has a trend similar to microparticle shear stress evolution [62] (Figure (17(b)).

4. Conclusion

In this work we had studied the influence of arteriolar hyperelasticity on artificial microparticle deformation, trajectory and velocity during the process of lateral migration. Furthermore, we examined the same influence on inter-particle hydrodynamic interactions. Results have revealed the presence of a lift-compensating suction force f_{DW} that modifies the overall microparticle dynamic in flow and brings

about a risk of accumulation near the wall. Deformation modes observed for the DAW are in good agreement with those reported in literature for rigid microchannels (i.e. tear-drop, ellipsoidal and slipper shapes). The suction force magnitude is confinement-dependent and stiffness-dependent, for larger microparticle the force is also viscosity ratio-dependent. Larger microparticle ($c = 0.5$), relatively stiff ($Ca = 0.02$) and whose viscosity is less than the carrying blood flow viscosity seems to be less sensitive to the aspiration and migrates easily.

Regarding the influence of the arteriolar distensibility on inter-particle interactions, the main findings include the process of overtaking ($c = 0.15$) and an extra deformation mode ($c = 0.5$). Interesting observations are also made for the RAW like clustering ($c = 0.5$), the highly pointed rear-end that tends to subdivide into two cusp-like instabilities and the presence of a suction force even in the absence of arteriolar distensibility ($c = 0.15$). Prescribing combinations of microparticle mechanical and rheological properties is necessary in microparticle design to anticipate risky situations in a medical context, in particular clustering and accumulation near the wall. Drawing on obtained results, the risk of aggregation could solely be

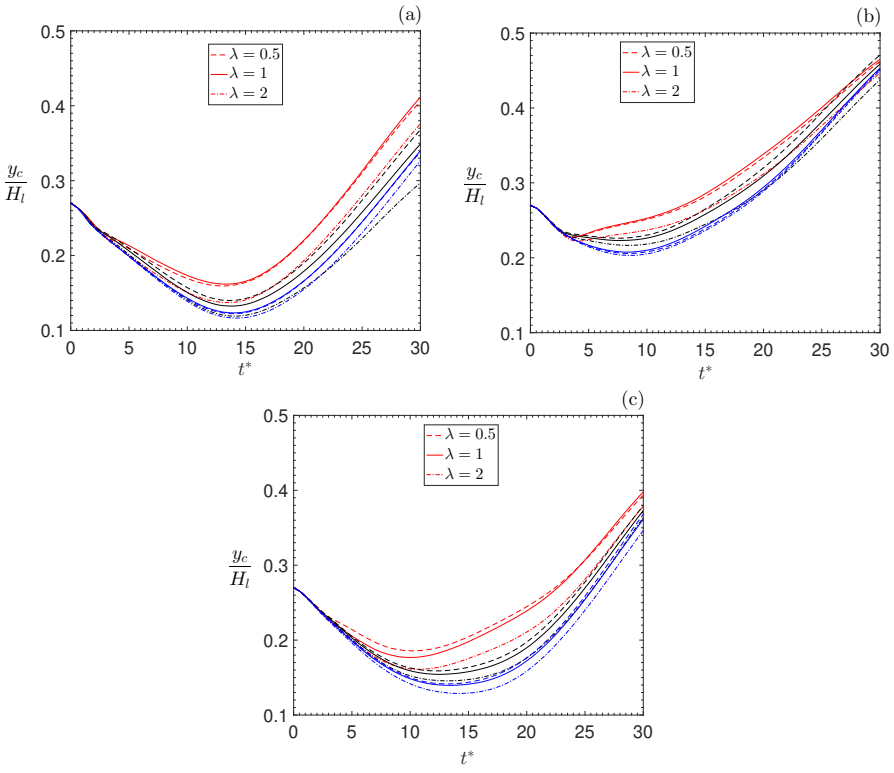

Fig. 12. Microparticles migration time evolution $c = 0.5$, DAW (a) Lg (b) Ld (c) Md. Red color is for $Ca = 0.5$, black for $Ca = 0.1$ and blue for $Ca = 0.02$.

discarded for $c = 0.15$ in the presence of the RAW. For this same combination, the risk of microparticles adhesion to wall is unexpectedly present and increases

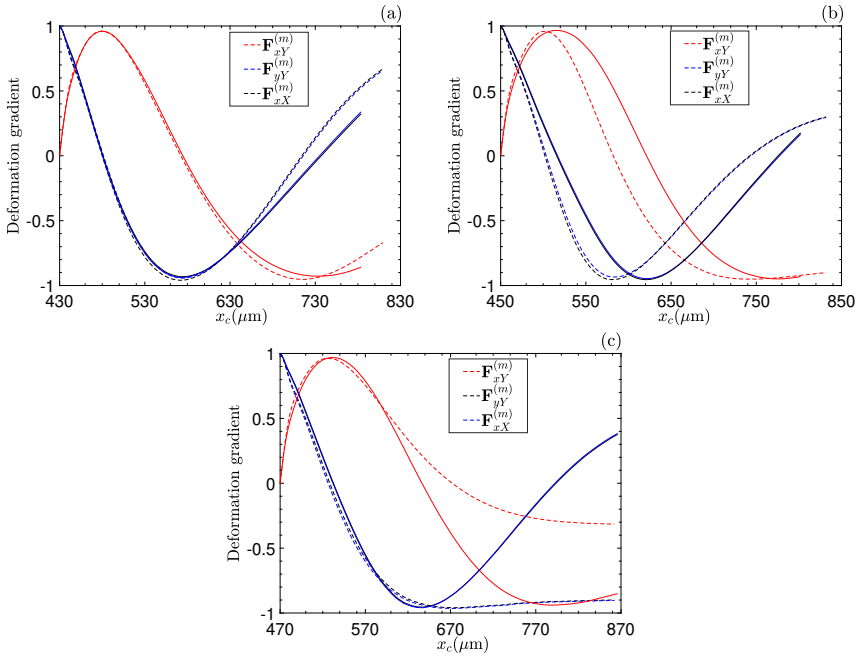

Fig. 13. Deformation gradient ($c = 0.5$, $Ca = 0.1$), x denotes the new location of the material particle and Y denotes the original one (and so on). Solid lines are for RAW and dashed lines for DAW (a) Lg (b) Md (c) Ld.

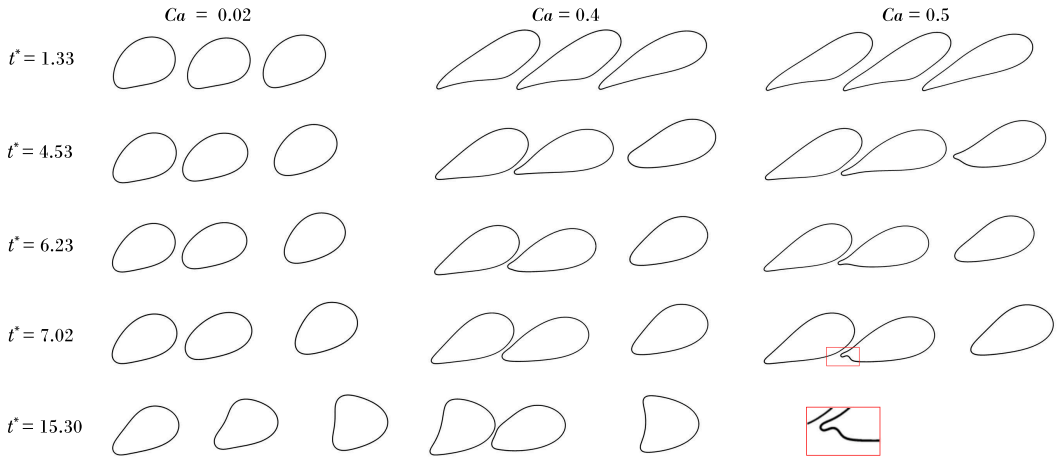

Fig. 14. Sequential snapshots of deformed shapes ($\lambda = 1$, RAW).

with increasing microparticle stiffness. Blood heterogeneity, larger amount of microparticles and various outflow conditions would provide a deeper knowledge of microparticle dynamics in human blood vessels.

Conflicts of Interest

There are no conflicts to declare.

References

1. Zhao Y, Li X, Zhao X, Yang Y, Li H, Zhou X, Yuan W, Asymmetrical Polymer Vesicles for Drug delivery and Other Applications, *Frontiers in Pharmacology* **8**:1–9, 2017.
2. Ma J, Du L F, Chen M, Wang H H, Xing L X, Jing L F, Li Y H, Drug-loaded nano-microcapsules delivery system mediated by ultrasound-targeted microbubble destruction: A promising therapy method (Review), *Biomedical Reports* **1**:506–510, 2013.
3. Chumakova O V, Liopo A V, Andreev V G, Cicenaite I, Evers B M, Chakrabarty S, Pappas T C, Esenaliev R O, Composition of PLGA and PEI/DNA nanoparticles improves ultrasound-mediated gene delivery in solid tumors in vivo, *Cancer Letters* **261**:215–225, 2008.

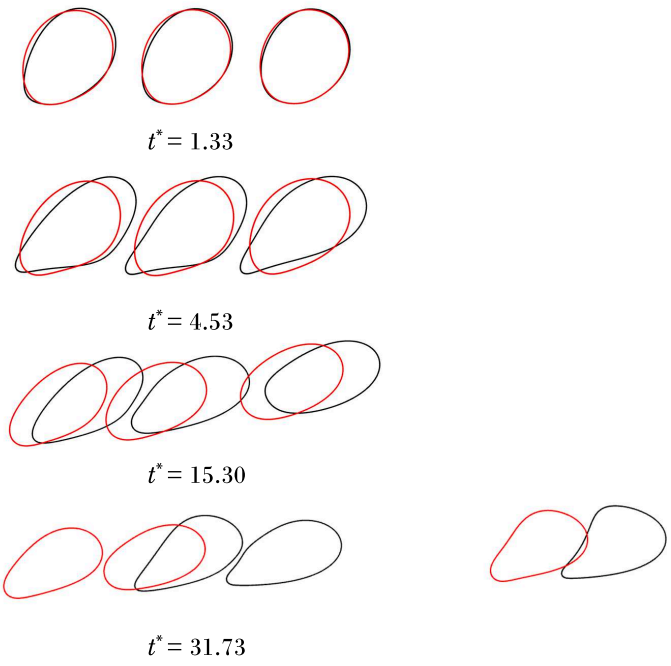

Fig. 15. Sequential snapshots of deformed shapes ($\lambda = 1$, DAW). Red color is for $Ca = 0.02$ and black for $Ca = 0.5$.

4. Mihalko E, Huang K, Sproul E, Cheng K, Brown A C, Targeted Treatment of Ischemic and Fibrotic Complications of Myocardial Infarction Using a Dual-Delivery Microgel Therapeutic, *ACS Nano* **12**:7826–7837, 2018.
5. Coupier G, Farutin A, Minetti C, Podgorski T, Misbah C, Shape Diagram of Vesicles in Poiseuille Flow, *Physical Review Letters* **108**, 2012.
6. Kaoui B, Coupier G, Misbah C, Podgorski T, Lateral migration of vesicles in microchannels: effects of walls and shear gradient, *La Houille Blanche* **5**:112–119, 2009.
7. Taylor R R, Tang Y, Gonzalez M V, Stratford P W, Lewis A L, Irinotecan drug eluting beads for use in chemoembolization: In vitro and in vivo evaluation of drug release

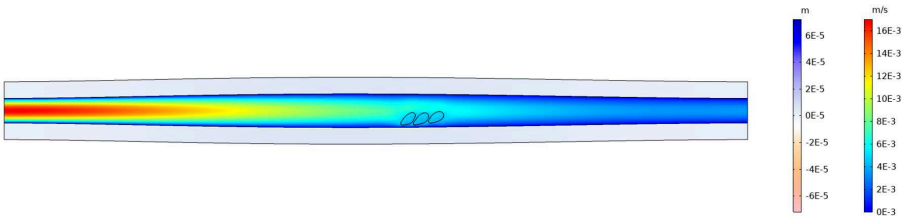

(a) $t^* = 8.5$

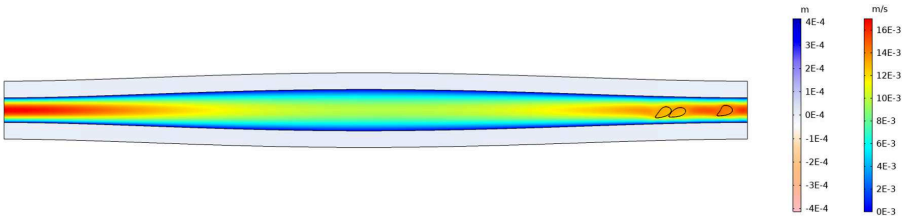

(b) $t^* = 31.17$

Fig. 16. Arteriolar dilation and microparticle lateral migration in the Poiseuille blood flow ($\lambda = 1$, $c = 0.5$, $Ca = 0.5$, DAW). The rainbow color table shows fluid velocity magnitude while the second one represents the vertical displacement of the solid domain.

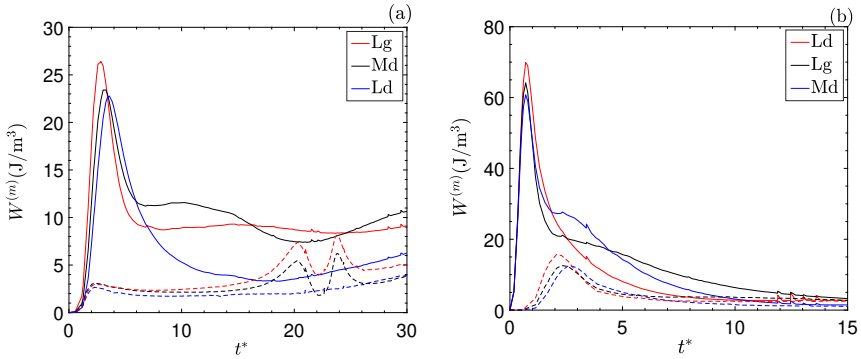

Fig. 17. Elastic energy density $\lambda = 1$ (a) $Ca = 0.1$, solid lines are for RAW and dashed lines are for DAW (b) $Ca = 0.5$, solid lines are for $c = 0.5$ and dashed lines for $c = 0.15$

properties, *European Journal of Pharmaceutical Sciences* **30**:7–14, 2007.
8. Fuchs K, Bize P E, Dormond O, Denys A, Doelker E, Borchard G, Jordan O, Drug-Eluting Beads Loaded with Antiangiogenic Agents for Chemoembolization: In Vitro Sunitinib Loading and Release and In Vivo Pharmacokinetics in an Animal Model, *Journal of Vascular and Interventional Radiology* **25**:379–387, 2014.
9. Khoo B L, Warkiani M E, Tan D S W, Bhagat A A S, Irwin D, Lau D P, Lim A S T, Lim K H, Krisna S S, Lim W T, Yap Y S, Lee S C, Soo R A, Han J, Lim C T, Clinical validation of an ultra high-throughput spiral microfluidics for the detection and enrichment of viable circulating tumor cells, *Plos One* **9**:1–7, 2014.
10. Browne A W, Ramasamy L, Cripe T P, Ahn C H, A lab-on-a-chip for rapid blood separation and quantification of hematocrit and serum analytes, *Lab on a Chip* **11**:2440–2446, 2011.
11. Carlo D D, Irimia D, Tompkins R G, Toner M, Continuous inertial focusing, ordering, and separation of particles in microchannels, *PNAS* **104**:18892–18897, 2007.
12. Zhu L, Rabault J, Brandt L, The dynamics of a capsule in a wall-bounded oscillating shear flow, *Physics of Fluids* **27**:1–16, 2015.
13. Nix S, Imai Y, Matsunaga D, Yamaguchi T, Ishikawa T, Lateral migration of a spherical capsule near a plane wall in Stokes flow, *Physical Review E* **90**, 2014.
14. Hariprasad D S, Secomb T W, Motion of red blood cells near microvessel walls: effects of a porous wall layer, *Journal of Fluid Mechanics* **705**:195–212, 2012.
15. Goldsmith H L, Mason S G, Axial Migration of Particles in Poiseuille Flow, *Nature* **190**:1095–1096, 1961.
16. Tam C K W, Hyman W A, Transverse motion of an elastic sphere in a shear field, *Journal of Fluid Mechanics* **59**:177–185, 1973.
17. Hou H W, Bhagat A A S, Chong A G L, Mao P, Tan K S W, Han J, Lim C T, Deformability based cell margination - A simple microfluidic design for malaria-infected erythrocyte separation, *Lab ob a Chip* **10**:2605–2613, 2010.
18. Namgung B, Ng Y C, Leo H L, Rifkind J M, Kim S, Near-Wall Migration Dynamics of Erythrocytes in Vivo: Effects of Cell Deformability and Arteriolar Bifurcation, *Frontiers in Physiology* **8**:1–10, 2017.
19. Schaaf C, Stark H, Inertial migration and axial control of deformable capsules, *Soft Matter* **13**:3544–3555, 2017.
20. Doddi S K, Bagchi P, Lateral migration of a capsule in a plane Poiseuille flow in a channel, *Lab ob a Chip* **34**:966–986, 2008.
21. He L, Luo Z, Liu W R, Bai B, Capsule equilibrium positions near channel center in Poiseuille flow, *Chemical Engineering Science* **172**:603–611, 2017.
22. Amini H, Lee W, Carlo D D, Inertial microfluidic physics, *Lab on a Chip* **14**:2739–2761, 2014.
23. Li H, Ma G, Modeling performance of a two-dimensional capsule in a microchannel flow: Long-term lateral migration, *Physical Review E* **82**:1–14, 2010.
24. Nix S, Imai Y, Ishikawa T, Lateral migration of a capsule in a parabolic flow, *Journal of Biomechanics* **49**:2249–2254, 2016.
25. Coclite A, Ranaldo S, Tullio M D, Decuzzi P, Pascazio G, Kinematic and dynamic forcing strategies for predicting the transport of inertial capsules via a combined lattice Boltzmann - Immersed Boundary method, *Computers and Fluids* **180**:41–53, 2019.
26. Beaucourt J, Biben T, Misbah C, Optimal lift force on vesicles near a compressible substrate, *Europhysics Letters* **67**:676–682, 2004.
27. El Jirari I, El Baroudi A, Ammar A, Numerical investigation of the dynamical behavior of a fluid-filled microparticle suspended in human arteriole, *Journal of Biomechanical Engineering* **143**, 2021.

28. Cheema T A, Park C W, Numerical investigation of hyperelastic wall deformation characteristics in a micro-scale stenotic blood vessel, *Korea-Australia Rheology Journal* **25**:121–127, 2013.
29. Brooks D E, Goodwin J W, Seaman G V, Interactions among erythrocytes under shear, *Journal of Applied Physiology* **28**, 1970.
30. San O, Staples A E, An improved model for reduced-order physiological fluid flows, *Journal of Mechanics in Medicine and Biology* **12**, 2012.
31. Westerhof N, Boer C, Lamberts R R, Sipkema P, Cross-talk between cardiac muscle and coronary vasculature, *Physiological Reviews* **86**, 2006.
32. Hu X Q, Salsac A V,and D. Barthès-Biesel D, Flow of a spherical capsule in a pore with circular or square cross-section, *Journal of Fluid Mechanics* **705**:176–194, 2012.
33. Leyrat-Maurin A, Barthes-Biesel D, Motion of a deformable capsule through a hyperbolic constriction, *Journal of Fluid Mechanics* **279**:135–163, 1994.
34. Knoche S, Kierfeld J, Buckling of spherical capsules, *Physical Review E* **84**, 2011.
35. Fery A, F Dubreuil F, Möhwald H, Mechanics of artificial microcapsules, *New Journal of Physics* **6**, 2004.
36. Jadhav S, Chan K Y, Konstantopoulos K, Eggleton C D, Shear modulation of intercellular contact area between two deformable cells colliding under flow, *Journal of Biomechanics* **40**, 2007.
37. Chu T X, Salsac A V, Leclerc E, Barthès-Biesel D, Wurtz W, Edwards-Lévy F, Comparison between measurements of elasticity and free amino group content of ovalbumin microcapsule membranes: Discrimination of the cross-linking degree, *Journal of Colloid and Interface Science* **355**:81–88, 2011.
38. Hirt C W, Amsden A A, Cook J L, An arbitrary Lagrangian-Eulerian computing method for all flow speeds, *Journal of Computational Physics* **14**:227–253, 1974.
39. Deuflhard P, A modified Newton method for the solution of ill-conditioned systems of nonlinear equations with application to multiple shooting, *Numerische Mathematik* **22**:289–315, 1974.
40. Smart J R, Leighton D T, Measurement of the drift of a droplet due to the presence of a plane, *Physics of Fluids A* **3**:21–28, 1991.
41. Mukherjee S, Sarkar K, Effects of matrix viscoelasticity on the lateral migration of a deformable drop in a wall-bounded shear, *Journal of Fluid Mechanics* **727**:318–345, 2013.
42. Chen Q, Patelli A, Chaté H, Ma Y, Shi X, Fore-aft asymmetric flocking, *Physical Review E* **96**, 2017.
43. Brooks A M, Sabrina S, Bishop J M, Shape-directed dynamics of active colloids powered by induced-charge electrophoresis, *Proceedings of the National Academy of Sciences of the United States of America* **115**:1090–1099, 2018.
44. Qiu T, Lee T, Mark A G, Morozov K I, Munster R, Mierka O, Turek S, Leshansky A M, Fischer P, Swimming by reciprocal motion at low Reynolds number, *Nature Communications* **5**, 2014.
45. Pak O S, Normand T, Lauga E, Pumping by flapping in a viscoelastic fluid, *Physical Review E* **81**, 2010.
46. Chan P C, Leal L G, The motion of a deformable drop in a second-order fluid, *Journal of Fluid Mechanics* **92**:131–170, 1979.
47. Ho B P, Leal L G, Migration of rigid spheres in a two-dimensional unidirectional shear flow of a second-order fluid, *Journal of Fluid Mechanics* **76**:783–799, 1976.
48. J. Matas J,and J. Morris J,and E. Guazzelli E, Lateral Forces on a Sphere, *Oil & Gas Science and Technology - Rev. IFP* **59**:59–70, 2004.
49. Moore D W, Saffman P G, The structure of free vertical shear layers in a rotating

fluid and the motion produced by a slowly rising body, *Philosophical Transactions of the Royal Society A* **264**, 1969.
50. Leach J, Mushfique H, Keen S, Leonardo R D, Ruocco G, Cooper J M, Padgett M J, Comparison of Faxen's correction for a microsphere translating or rotating near a surface, *Physical Review E* **79**, 2009.
51. Magnaudet J, Takagi S, Legendre D, Drag, deformation and lateral migration of a buoyant drop moving near a wall, *Journal of Fluid Mechanics* **476**:115–157, 2009.
52. Skalak R, Branemark P I, Deformation of red blood cells in capillaries, *Science* **164**, 1969.
53. Tomaiuolo G, Lanotte L, Ghigliotti G, Misbah C, Guido S, Red blood cell clustering in Poiseuille microcapillary flow, *Physics of Fluids* **24**, 2012.
54. Noguchi H, Gompper G, Shape transitions of fluid vesicles and red blood cells in capillary flows, *Proceedings of the National Academy of Sciences* **102**:14159-14164, 2005.
55. Kaoui B, Biros G, Misbah C, Why do red blood cells have asymmetric shapes even in a symmetric flow, *Physical Review Letters* **103**, 2009.
56. Miura H, Wachtel R E, Liu Y, Loberiza F R, Saito T, Miura M, Gutterman D D, Flow-induced dilation of human coronary arterioles important role of ca(2^+)-activated k(+) channels, *Circulation* **103**:1992–1998, 2001.
57. Zhang J, Yan S, Yuan D, Alici G, Nguyen N, Warkianic M E, Li W, Fundamentals and applications of inertial microfluidics: A review, *Lab on a chip* **16**:10–34, 2016.
58. Gao T, Hu H H, Deformation of elastic particles in viscous shear flow, *Journal of Computational Physics* **228**:2132–2151, 2009.
59. Lee K, Wagner C, Priezzhev A V, Assessment of the "cross-bridge"-induced interaction of red blood cells by optical trapping combined with microfluidics, *Journal of Biomedical Optics* **22**, 2017.
60. Misbah C, Vesicles, capsules and red blood cells under flow, *Journal of Physics: Conference Series* **392**:1–17, 2012.
61. Bryngelson S H, Freund J B, Global stability of flowing red blood cell trains, *Physical Review Fluids* **3**, 2018.
62. H. Zhao H, Shaqfeh E S G, The dynamics of a non-dilute vesicle suspension in a simple shear flow, *Journal of Fluid Mechanics* **725**:709-731, 2013.